Geophysical Research Letters

RESEARCH LETTER
10.1029/2019GL086668

Spatiotemporal Seismic Structure Variations Associated With the 2018 Kīlauea Eruption Based on Temporary Dense Geophone Arrays

Sin-Mei Wu[1], Fan-Chi Lin[1,2], Jamie Farrell[1], Brian Shiro[3], Leif Karlstrom[4], Paul Okubo[3], and Keith Koper[1]

[1]Department of Geology and Geophysics, University of Utah, Salt Lake City, UT, USA, [2]Institute of Earth Sciences, Academia Sinica, Taipei, Taiwan, [3]Hawaiian Volcano Observatory, U.S. Geological Survey, Hilo, HI, USA, [4]Department of Earth Sciences, University of Oregon, Eugene, OR, USA

Key Points:
- Temporary seismic array targeting ongoing eruptive activity permits studies on dynamics between preexisting and newly formed structures
- We observe spatially dependent seismic velocity variations associated with the newly intruded dike emplacement in the lower East Rift Zone
- Magma pressurization and its transmission through the hydraulically connected dike can be monitored from crustal seismic velocity

Supporting Information:
- Supporting Information S1

Correspondence to:
S.-M. Wu,
sinmei.wu@utah.edu

Citation:
Wu, S.-M., Lin, F.-C., Farrell, J., Shiro, B., Karlstrom, L., Okubo, P., & Koper, K. (2020). Spatiotemporal seismic structure variations associated with the 2018 Kīlauea eruption based on temporary dense geophone arrays. *Geophysical Research Letters*, *47*, e2019GL086668. https://doi.org/10.1029/2019GL086668

Received 16 DEC 2019
Accepted 21 APR 2020
Accepted article online 23 APR 2020
Corrected 3 JUNE 2020

This article was corrected on 3 JUNE 2020. See the end of the full text for details.

Abstract During the 2018 Kīlauea volcanic eruption, lava erupted from a series of new fissures in the lower East Rift Zone more than 30 km away from the summit through a dike intrusion. Between late May and early August, variations in the effusion rate at the persistent eruptive vent (Fissure 8) were observed following near-daily summit caldera collapse events. Targeting the ongoing eruptive activity and the subsurface magma movement, we deployed a temporary dense seismic array. The observed time-lapse changes in seismic velocity associated with the response of the summit collapse in three areas are presented in this study. The results show (1) clear spatially dependent co-collapse velocity reductions across the newly-intruded dike structure, (2) a gradual post-collapse velocity increase near Fissure 8 correlated with the surge of magma supply, and (3) a gradual post-collapse velocity increase on the summit likely associated with reservoir pressurization and crustal welding.

Plain Language Summary Volcanic eruptions commonly involve failure of rocks surrounding the subsurface magma transport system, such as fracturing and rupturing. During the 2018 Kīlauea volcano eruption, lava mainly erupted from new fissures within the lower East Rift Zone (LERZ) located tens of kilometers away from the magma reservoir beneath the summit. As magma drained from the summit system to feed the LERZ eruption, the summit caldera subsided in an episodic fashion through a series of 62 collapses. Despite this spatial separation, we observe correlation between the summit collapse and the LERZ eruptive activity suggesting the two features are interconnected through a subsurface dike. To better study the eruption dynamics and subsurface magma movement, we deployed a temporary dense seismic array across the Kīlauea volcano system during the steady phase after mid-June in 2018. In this study, we present the time-lapse changes in crustal seismic velocity observed across the dense array correlated with the summit collapses. We show that different volcanic components (i.e., summit, dike, and fissure) react to summit magma pressurization differently. Our findings provide new constraints on the time-evolving mechanical structure of a volcano during a major eruption.

1. Introduction

Since 1983, eruptions from Kīlauea volcano mainly occurred at the Halema'uma'u crater on the summit and Pu'u 'Ō'ō, a persistent vent on the East Rift Zone (ERZ) located ~20 km downrift from the summit (Heliker & Mattox, 2003; Orr et al., 2015; Patrick et al., 2018; Poland et al., 2014; Wolfe, 1988). The magma is supplied by a reservoir 1–2 km beneath the summit (Anderson et al., 2019; Denlinger, 1997; Poland et al., 2014; Patrick, Orr, et al., 2019). On 1 May (UTC time), migration of seismicity and ground deformation indicated that a dike intruded ~20 km downrift of Pu'u 'Ō'ō to the lower East Rift Zone (LERZ) (Neal et al., 2019). Following the intrusion, 24 new eruptive fissures opened and eventually coalesced around Fissure 8, which became the principal outlet of lava between late May and early August (Figure 1). Coincident in time with Fissure 8's activity, collapse events equivalent to magnitude 5.2–5.4 on the Kīlauea summit occurred nearly daily (Neal et al., 2019).

The summit collapse events, presumably accommodated by a ring-fault system which developed during middle to late June (Segall et al., 2019), were triggered by progressive magma withdrawal from the 1- to 2-km-deep summit reservoir (Anderson et al., 2019; Liang et al., 2020). The collapse of the caldera roof

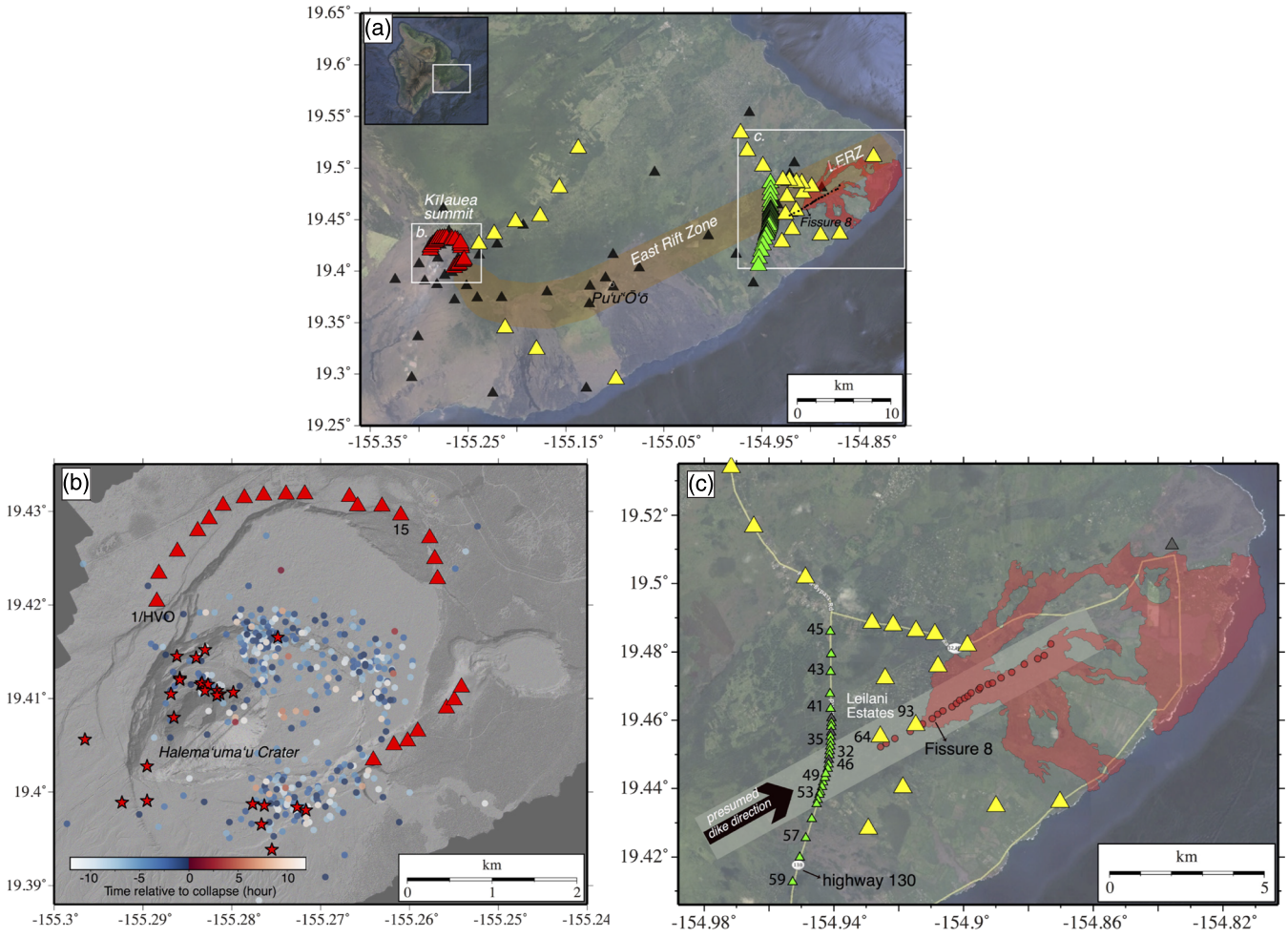

Figure 1. (a) Map of geographic features and the seismic nodal array (colored triangles) deployed between mid-June and mid-July 2018 on the island of Hawai'i. Locations of permanent seismic stations (black triangles) are also shown for reference. Orange area indicates East Rift Zone; light red area illustrates the active lava flows during 2018 eruption (Neal et al., 2019). The white rectangles denote the areas of enlargement shown in Figures 1b and 1c. (b) The magnified map showing the summit nodal array (triangles) and seismicity distribution based on standard USGS catalog (Shiro et al., 2018). Red stars denote the ~*M*5 collapse events; the earthquakes (circles) are color coded by the occurrence time relative to the closest collapse event. (c) The magnified map showing the LERZ nodal array (triangles) and hypothesized dike emplacement (light gray area). Yellow lines are roads. Red circles are the eruptive fissures during the 2018 eruption. Fissure 8 is the active fissure during the nodal deployment. Problematic stations not used in this study are marked as gray triangles (Text S1 in the supporting information).

pressurized the underlying magma reservoir, increased magma flux in the dike, and led to higher effusion rates at Fissure 8 (Neal et al., 2019; Patrick, Dietterich, et al., 2019). The observed correlation between summit deformation and increased effusion rates at Fissure 8 thus suggests that the two were hydraulically connected. The early stages of the eruption were accompanied by vigorous seismicity, which outlined the geometry and progression of the initial dike intrusion. After the establishment of the long-lived erupting vent (Fissure 8) as an "open pipe," seismicity in the LERZ decreased significantly (Shiro et al., 2018). To further understand the hydraulic connection and the dynamics of the magma movement during the nearly steady state eruption stage, other high-resolution measurements in both space and time are needed.

In this study, we investigate the temporal changes in seismic velocity across Kīlauea volcano associated with the 2018 eruption to infer the dynamic response to summit collapse events. We use data from a dense seismic array we deployed from mid-June through mid-July 2018 (Lin & Farrell, 2018), which recorded 25 out of the 62 summit collapses (Figure 1). Recently, dense seismic arrays have been widely used to image detailed crustal structure (e.g., Lin et al., 2013; Nakata et al., 2015; Schmandt &

Clayton, 2013; Wang et al., 2019; Ward et al., 2018; Wu et al., 2017) and monitor ongoing volcanic and hydrothermal activity (Donaldson et al., 2017; Obermann et al., 2013; Olivier et al., 2019; Wu et al., 2019). Here we apply coda wave interferometry (Snieder et al., 2002) to the seismic noise recordings. This technique permits the detection of small changes in the seismic velocity of the propagation medium, through changes in the noise correlation coda. Previous studies have successfully applied this technique to volcano monitoring (e.g., Bennington et al., 2018; Donaldson et al., 2017; Haney et al., 2015; Obermann et al., 2013; Olivier et al., 2019) and investigation of crustal damage/recovery following large earthquakes (e.g., Brenguier et al., 2008; Wegler et al., 2009). Recently, the technique was applied to investigate the long-term inflation/deflation associated with the Kīlauea magma reservoir (Donaldson et al., 2017) and short-term structural damage that occurred ~10 days prior to the 2018 Kīlauea eruption (Olivier et al., 2019). We find clear, space- and time-dependent velocity changes likely associated with crustal damage, strengthening, and relaxation in response to the summit collapse events and hence infer the reservoir pressurization and dynamic stress variations.

2. Data

In response to the 2018 Kīlauea eruption, the University of Utah partnered with the U.S. Geological Survey Hawaiian Volcano Observatory to deploy a dense geophone array between 15 June and 26 July 2018 (Lin & Farrell, 2018). The array was composed of 80 three-component autonomous 5-Hz nodal geophone stations (Ringler et al., 2018; Text S1) that continuously recorded with a 250-Hz sampling rate. There were two subarrays targeting the Kīlauea summit and the LERZ (Figure 1a). The summit subarray consisted of 24 stations with ~250-m station spacing partially encircling the summit caldera (Figure 1b). The LERZ subarray (Figure 1c) consisted of 30 closely spaced stations (~200-m spacing near the center) along highway 130 crossing the presumed subsurface dike structure (Neal et al., 2019; Poland et al., 2014). Another 16 stations were distributed in and around Leilani Estates near the active lava fountaining and surface lava flow. We note that Station 93 is closest to Fissure 8, located just ~700 m away. In addition to the two major subarrays, nine geophones were deployed in accessible locations around the ERZ. Bad stations and other deployment problems are documented in Text S1.

During the nodal deployment, the Kīlauea summit experienced 25 near-daily M5.2 to M5.4 collapse events with an ~30-hr average interval. The collapse events were accompanied by a distinct seismicity cycle where summit seismicity dropped immediately after the collapse, followed by an ~10-hr quiescent period, and increased gradually before the next collapse (Figure 1b). Epicenters of the collapse events are predominantly located east of Halema'uma'u particularly focused on the NE side (Figure 1b). While extensive seismicity occurred at the Kīlauea summit, the LERZ was seismically quiet during the array experiment, with the exception of potential signals from continuous fountaining at Fissure 8 and littoral blasts from the ocean entry.

3. Methods

We apply coda wave interferometry to autocorrelation functions (ACFs) of seismic noise (Minato et al., 2012; Yu & Hung, 2012) to investigate the temporal and spatial variations of crustal elastic properties in response to the summit collapse and underground magma flow. After removing the instrument response to generate ground velocity, we downsample the daily seismograms to 50 samples per second, remove the mean and trend, and divide the data into 5-min segments. The results of this study are presented in two time resolutions: 5 min (no stacking) and 1 hr (stacking). For the hourly stacking ACF, we first apply a Butterworth filter between 1 and 5 Hz to remove high-frequency energy and then normalize each 5-min ACF by its maximum amplitude before the stacking process. We stack 12 consecutive 5-min ACFs to retrieve the hourly stacking ACF and use the start of each hour as the representative time. To better observe the signals in response to the collapse events, all the ACFs are organized chronologically relative to the event origin times. Coherent coda signals, which are the bases for our interferometric analysis, can be observed in ACFs both before and after the collapse events (Figure S1).

The relative velocity is measured using a moving-window cross-spectral technique between any two given ACFs from the same station but different time periods (Poupinet et al., 1984; Yu & Hung, 2012). Assuming evenly distributed scatters and a homogenous velocity perturbation, this technique estimates

the linear relationship between the time lag ($\delta\tau$) and lapse time (τ) of coda signals, which is inversely related to the fractional perturbation in seismic velocity ($\delta v/v$). We use a 50% overlapping 2-s moving window between 2- and 12-s lapse time to determine the time shifts and hence the velocity perturbation. Rather than choosing an arbitrarily long-time averaged ACF as a reference, we adopt the Bayesian least squares inversion technique from Brenguier et al. (2014; Text S2) and use any combination of the ACFs to construct the final time-lapse velocity variation. Thus for each station, ~2 million $\delta v/v$ measurements contribute to the final result.

4. Results and Discussion

Figures 2–4 summarize the results of temporal velocity variations ($\delta v/v$) in the following locations: (1) above the LERZ dike emplacement, (2) near Fissure 8, and (3) at the Kīlauea summit. Here, the variations in $\delta v/v$ are expressed relative to the onsets of the 25 collapse events recorded during the array deployment. We calculate the average velocity perturbations combined for all collapse events and estimate a 95% confidence region to determine the dominant pattern common to all collapse events (Figure S2).

4.1. LERZ Dike Emplacement

Here we present the $\delta v/v$ at stations of the dense linear array along highway 130 in the LERZ (Figure 1c). The intersection between the dike and the array is likely near the middle of the array (between Stations 46 and 49) where elevated temperatures, SO_2 gas emissions, intense ground cracking, and extensive steam vapor emission were present (Figures 1c and 2b). Strong ground motion excited by the collapse events is also observed near the center of our linear array with the largest peak ground velocity (PGV) observed about 1 km north of the dike (Figure S3c). The spatial PGV pattern suggests the presence of a low seismic velocity anomaly adjacent to the dike with induced wave focusing and amplification.

The $\delta v/v$ results exhibit a clear co-collapse seismic velocity drop with a distinct spatial pattern in magnitude associated with the presumed underground dike location (Figures 2 and S3a). The velocity drop has a maximum magnitude of −0.27% (±0.03%) at Station 46 near the middle of the array and gradually decreases in magnitude toward both sides. For each station, the sudden velocity drop is followed by an exponential recovery, which closely resembles previous observations of dynamic crustal weakening/damage following large earthquakes ($M > 7$; Brenguier et al., 2008; Nakata & Snieder, 2011 ; Peng & Ben-Zion, 2006). We also attribute the sudden velocity drop to dynamic weakening (damage from strong shaking) based on its spatial correlation with the observed PGV pattern (Figure S3c). However, we cannot completely rule out the potential contribution from stress changes associated with magma flux variations within the underlying dike.

To further quantify the spatiotemporal pattern of observed $\delta v/v$, for each station, we determine the co-collapse velocity drop and the 90% exponential relaxation/recovery time (i.e., the velocity recovers to 90% of its pre-collapse value) based on least squares curve fitting (Text S3). Note that previous studies utilized a logarithmic model for postseismic recovery which usually lasts over months and commonly has permanent change (Nakata & Snieder, 2011; Peng & Ben-Zion, 2006). In contrast, the observations in this study explicitly show full recovery within hours of the collapse. Here, we employ a simple exponential recovery model to avoid the divergence of the logarithmic model and ensure that the modeled velocity returns to its reference level (Hobiger et al., 2014; Qiu et al., 2019; Snieder et al., 2016; Taira et al., 2018). In Figures S3a and S3b, we plot the estimated velocity drops and relaxation times as a function of orthogonal station distance to the surface projection of the linear dike. The result shows a clear asymmetrical zone of significant velocity drops (>0.1%) with a width of ~500 m to the south and ~1,500 m to the north (gray area in Figure S3). This width is slightly larger than our estimated lateral resolution (Text S4) assuming a Rayleigh wave dominant background wavefield (Text S5 and Figures S4 and S5). Despite some scattered points, stations north of Station 46 in general have a shorter relaxation time (<2 hr) compared to stations to the south (Figure S3b).

The slight spatial offset between the patterns of the $\delta v/v$ drop and PGV suggests that the medium in the immediate vicinity of the dike is more susceptible to dynamic weakening (Brenguier et al., 2014). Estimation from Poland et al. (2014) and Neal et al. (2019) suggests the dike emplacement is at ~2–4 km deep with an ~2- to 4-m opening in the ERZ, which is deeper than the expected sensitivity of our measurements (Text S4). It is possible that the dike emplacement was closer to the surface in the LERZ as it shallowed closer

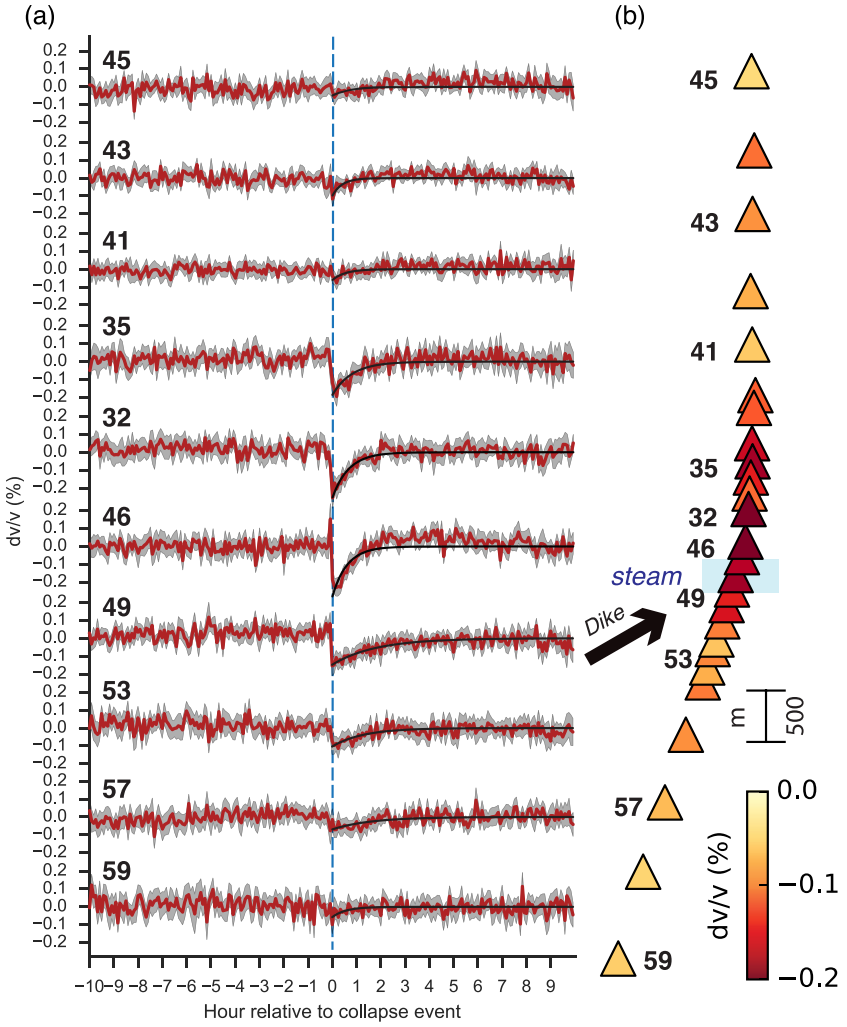

Figure 2. (a) Velocity drop and recovery across the LERZ associated with summit collapses. The velocity variations are retrieved from nonoverlapping 5-min time windows. The red lines and the gray areas represent averaged velocity and 95% confidence intervals from ~25 collapse events. The black lines represent the best fitting curves for co-collapse velocity drop and exponential recovery. The blue-dashed line marks the collapse event reference time. Labeled numbers correspond to station locations shown in Figures 1c and 2b. (b) Station locations (triangles) are along Highway 130, which are color coded by the co-collapse velocity drops from the best fitting results, showing clear spatial pattern related to the subsurface dike structure. The blue area indicates vapor steam, elevated temperatures, and gas emissions observed on the surface.

to the surface eruption, which fractured the shallow crust, making it more susceptible to further weakening, and also increased the shallow hydrothermal steam venting.

The asymmetry of the velocity drop, relaxation time, and PGV (Figures 2 and S3) suggests the dike may serve as a physical boundary (e.g., separating two different stress regions), the dike emplacement occurred at a pre-existing structural boundary, or the dike structure is itself asymmetric. We note that differences in densities from previous lava flows from previous eruption episodes have been reported (Clague et al., 1999; Hagstrum & Champion, 1994) and a buttressed north flank and a more mobile south flank have also been inferred (Denlinger & Okubo, 1995; Montgomery-Brown et al., 2009; Owen et al., 2000; Swanson et al., 1976).

4.2. LERZ Fountain Eruption (Fissure 8)

We present the hourly stacked $\delta v/v$ at three stations that were in line with the linearly distributed fissures in the LERZ (Figure 1c). These three stations, 46, 64, and 93, were 3.8, 1.9, and 0.7 km from Fissure 8, respectively. The results at Stations 46 and 64 show clear co-collapse velocity drops of around −0.2% that are

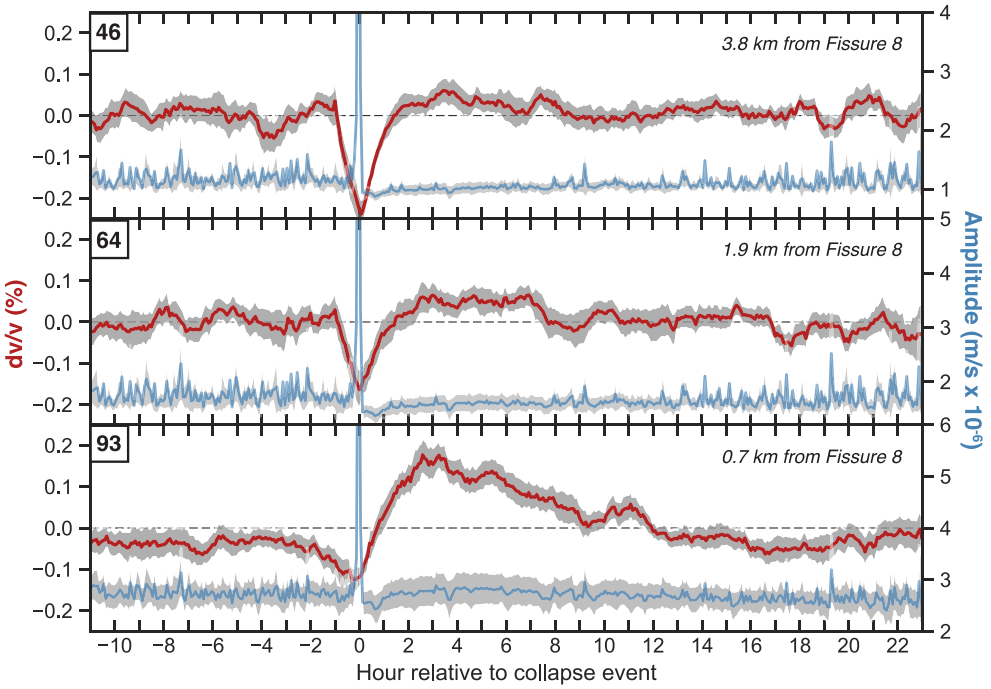

Figure 3. Seismic velocity variations measured at Stations 46, 64, and 93 (upper left insects; Figure 1c) in the LERZ associated with Kīlauea summit collapses. The velocity variations are retrieved from smoothed hourly stacked ACFs, yielding the affected velocity variation 1-hr preceding the exact perturbed time. The red and blue lines represent averaged velocity perturbations and recorded seismic ground motion amplitudes (5-min resolution) among ~25 collapse events, respectively. The gray areas indicate the 95% confidence intervals. Black dashed lines mark the level of unperturbed velocity level.

associated with structural weakening and an ~1.5-hr 90% recovery time (Figure 3). We note that the apparent velocity drop starting ~1 hr before the collapse is introduced by hourly stacking for enhancing the signal-to-noise ratio. In addition to the co-collapse velocity drop similar to that observed at Stations 46 and 64, Station 93 exhibited an increase in velocity with a peak ~2–3 hr after the collapse event (Figure 3). The apparent peak velocity perturbation of 0.18 ± 0.05% is followed by an exponential decay where $\delta v/v$ returns to the unperturbed condition ~12 hr after the collapse. The velocity increase is likely associated with the crack-closing process while the crust was under compression. Such an effect has been observed at the Kīlauea summit during the cyclic deflation/inflation induced by the magma reservoir's pressurization (Donaldson et al., 2017). Based on the observation of higher effusion rates at Fissure 8 following the summit collapses (Patrick, Dietterich, et al., 2019), we hypothesize that the magma influx surge within the LERZ shallow magma plumbing system contributes to the pressurization.

In this conceptual model, the summit collapse events act as piston drops and the summit magma reservoir is hydraulically connected to the ERZ/LERZ dike plumbing system (Anderson et al., 2019; Gudmundsson et al., 2016; Neal et al., 2019). The 2- to 3-hr lag time for the maximum velocity increase may be related to the transit time for the surge of magma influx to migrate down to Fissure 8, around 40 km away (Patrick, Dietterich, et al., 2019). A 2- to 3-hr delay in peak effusion rates following pressurization at one end requires a compliant and elastic-walled dike structure (Bokhove et al., 2005). Note that we do not have the temporal resolution to determine the onset of the effusion increase, which likely happened within 20 min after the collapse (Patrick, Dietterich, et al., 2019). Comparison of characteristic transit time for pressure diffusion associated with magma flow through an elastic-walled dike (Montagna & Gonnermann, 2013; Figure S6), to flux from Fissure 8, suggests a dike width between 1 and 3 m. There is a trade-off between dike height, shear modulus, Poisson's ratio of the host rocks, and magma viscosity to control pressure diffusivity so it is less well constrained (Text S6). The exponential velocity relaxation after the peak $\delta v/v$ increase will scale with the decreasing source pressure driving excess flow in the dike (Woods & Huppert, 2003). While the structural weakening from the collapse is

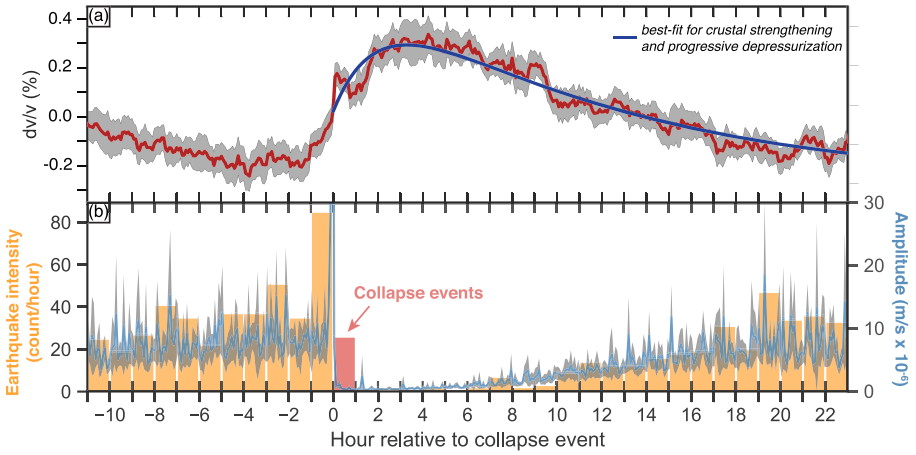

Figure 4. (a) Seismic velocity variations associated with Kīlauea summit collapse events measured at Station 15 on the NE rim of the summit caldera. The velocity variations are retrieved from hourly stacked ACFs, yielding the affected velocity variation 1 hr preceding the exact perturbed time. The red line represents averaged velocity among ~25 collapse events and the gray area indicates the 95% confidence interval. The blue line represents the best fit curve account for both structural weakening from longer time scale depressurization and crustal strengthening from instantaneous collapse pressurization. (b) Earthquake counts (orange histogram) on the summit between 15 June and 19 July 2018 relative to collapse times. The blue lines and the gray area represent averaged seismic amplitudes with 5-min resolution and its 95% confidence interval, respectively.

ubiquitous in the vicinity of the LERZ, the pressurization-induced velocity increase is clearest near Fissure 8. This suggests the intruded magma pathway reaches a shallower depth very near Fissure 8, and the shallow crustal velocity is sensitive to dynamic pressures in the magma. Alternatively, the change from a Rayleigh wave to body wave dominant wavefield (Figure S5) might extend the depth sensitivity of our measurements (Text S4). We note that Station 93 has a higher overall seismic ground motion amplitude when compared with other stations within the LERZ (Figure 3), particularly after the collapse events, likely related to the fountaining at Fissure 8.

4.3. The Kīlauea Summit

Variation in $\delta v/v$ at the station NE of the summit caldera (Station 15; Figure 1b) exhibited a gradual increase of $0.34 \pm 0.08\%$ maximum amplitude, peaking ~4 hr after the collapse (Figure 4). The velocity increase likely indicates compression of the shallow crust and is consistent with the contemporary GPS displacement measurement (Segall et al., 2019) and the previous strain model based on a dilated/pressurized magma reservoir at ~1-km depth (Donaldson et al., 2017). As the pressurization on the summit is considered to be instantaneous following collapse events (supported by abrupt changes in the GPS and tilt measurements in the vicinity of Halema'uma'u crater; Neal et al., 2019; Segall et al., 2019), the gradual velocity increase likely reflects the relaxation time of crustal strengthening/welding associated with crack realignment and closing (Brenguier et al., 2008; Snieder et al., 2016). Following collapse events, the reservoir gradually depressurized as magma flowed to the LERZ (Anderson et al., 2019). Such a depressurization process is consistent with the observed exponential relaxation in velocity. Therefore, the observed apparent velocity variation likely represents the superposition of these two processes with distinct scales in time: (1) crustal strengthening after the pressurization collapse event, occurring over a short time scale; and (2) crustal weakening due to depressurization, occurring over a longer time scale.

The magnitudes and relaxation times of the two effects that best fit the data are estimated using least squares curve fitting (Text S3 and Figure S7; blue line in Figure 4). The result suggests a $0.63 \pm 0.04\%$ co-collapse $\delta v/v$ increase from instantaneous pressurization with a 4.59 ± 0.18-hr strengthening/welding process followed by a 26.62 ± 2.04-hr weakening/depressurization process. The ~26-hr recovery time scale from depressurization is similar to the average collapse event interval (~30 hr) using all 25 collapse events, showing that shallow crustal weakening was in concert with the dynamic process of ongoing summit collapse. This is also supported by the decrease in velocity at a rate of ~−0.01% per hour and gradual increase in seismicity

preceding each collapse event, which is likely associated with the overall depressurization of the system due to the magma removal. We note that our $\delta v/v$ result from different summit stations shows a distinct spatial pattern characterized by a maximum apparent velocity increase in the NE section (Figure S8). The exact mechanism that causes this spatial variation is beyond the scope of this study and will be the subject of future studies. While the overall background seismic amplitude observed across the summit is clearly affected by nearby seismicity (Figure 4), no obvious wavefield characteristic change (Figure S5) that can potentially bias our result, has been observed during the collapse event cycle.

5. Conclusion

We designed and deployed a dense seismic array on Kīlauea volcano from mid-June through mid-July 2018. Using seismic noise coda wave interferometry, we investigated changes in seismic velocity in response to summit collapse events and inferred magmatic movement between the summit and the LERZ. Across the LERZ dike, we observed a clear co-collapse rapid $\delta v/v$ reduction followed by an exponential recovery. A maximum velocity drop of $-0.27 \pm 0.03\%$ is observed immediately above the presumed dike structure, which is likely most susceptible to dynamic weakening. Adjacent to Fissure 8, a gradual velocity increase with $\sim 0.18 \pm 0.05\%$ maximum amplitude is observed ~2–3 hr after the collapse. We interpret this as the surge of magma influx within the shallow plumbing system in response to summit reservoir pressurization. At the summit, a gradual $\delta v/v$ increase is also observed with $0.34 \pm 0.08\%$ maximum amplitude which peaks ~4 hr after the collapse. This velocity increase at the summit may be related to the exponential relaxation process of rock healing/crack closing in response to the instantaneous pressurization of the system at the time of the collapse event.

The results suggest that the elastic properties in the shallow crust of Kīlauea volcano varied in concert with the dynamics of magmatic activity at depth. These properties can be detected and monitored if instruments are close to the volcanic structure. We show that a dense seismic array can provide valuable new information on spatiotemporal variations of crustal structure which can then be used to monitor ongoing eruption activity. Future studies of high-resolution static velocity structure of the dike and summit by combining both temporary and permanent networks can advance our understanding of Kīlauea's magmatic plumbing system.

Acknowledgments
The authors thank the Hawaiian Volcano Observatory for providing collaborative support and field personnel. Data collection was performed under Hawai'i Volcanoes National Park permit HAVO-2018-SCI-0037. We would like to thank Matt Patrick, Alicia Hotovec-Ellis, Matt Haney, and two anonymous reviewers for insightful reviews, which helped to improve this manuscript. In addition, we thank Kyle Anderson for helpful discussions and Matthew Miller and Jefferson Chang for help with the field deployment. This research is supported by NSF EAR-1839100, EAR-1760094, EAR-1753362, and CyberSEES-1442665. L. K. acknowledges support from NSF Award EAR-1624557. The Lidar image is acquired from OpenTopography. The seismic data used in this study are archived at the IRIS DMC (https://doi.org/10.7914/SN/Z1_2018).

References

Anderson, K. R., Johanson, I. A., Patrick, M. R., Gu, M., Segall, P., Poland, M. P., et al. (2019). Magma reservoir failure and the onset of caldera collapse at Kīlauea Volcano in 2018. *Science*, *366*(6470), eaaz1822. https://doi.org/10.1126/science.aaz1822

Bennington, N., Haney, M., Thurber, C., & Zeng, X. (2018). Inferring magma dynamics at Veniamin of volcano via application of ambient noise. *Geophysical Research Letters*, *45*, 11–650. https://doi.org/10.1029/2018GL079909

Bokhove, O., Woods, A. W., & de Boer, A. (2005). Magma flow through elastic-walled dikes. *Theoretical and Computational Fluid Dynamics*, *19*(4), 261–286.

Brenguier, F., Campillo, M., Hadziioannou, C., Shapiro, N. M., Nadeau, R. M., & Larose, E. (2008). Postseismic relaxation along the San Andreas fault at Parkfield from continuous seismological observations. *Science*, *321*(5895), 1478–1481. https://doi.org/10.1126/science.1160943

Brenguier, F., Campillo, M., Takeda, T., Aoki, Y., Shapiro, N. M., Briand, X., et al. (2014). Mapping pressurized volcanic fluids from induced crustal seismic velocity drops. *Science*, *345*(6192), 80–82. https://doi.org/10.1126/science.1254073

Clague, D. A., Hagstrum, J. T., Champion, D. E., & Beeson, M. H. (1999). Kīlauea summit overflows: Their ages and distribution in the Puna District, Hawai'i. *Bulletin of Volcanology*, *61*(6), 363–381.

Denlinger, R. P. (1997). A dynamic balance between magma supply and eruption rate at Kilauea volcano, Hawaii. *Journal of Geophysical Research*, *102*(B8), 18,091–18,100.

Denlinger, R. P., & Okubo, P. (1995). Structure of the mobile south flank of Kilauea Volcano, Hawaii. *Journal of Geophysical Research*, *100*(B12), 24,499–24,507.

Donaldson, C., Caudron, C., Green, R. G., Thelen, W. A., & White, R. S. (2017). Relative seismic velocity variations correlate with deformation at Kīlauea volcano. *Science Advances*, *3*(6), e1700219. https://doi.org/10.1126/sciadv.1700219

Gudmundsson, M. T., Jónsdóttir, K., Hooper, A., Holohan, E. P., Halldórsson, S. A., Ófeigsson, B. G., et al. (2016). Gradual caldera collapse at Bárdarbunga volcano, Iceland, regulated by lateral magma outflow. *Science*, *353*(6296), aaf8988. https://doi.org/10.1126/science.aaf8988

Hagstrum, J. T., & Champion, D. E. (1994). Paleomagnetic correlation of Late Quaternary lava flows in the lower east rift zone of Kilauea Volcano, Hawaii. *Journal of Geophysical Research*, *99*(B11), 21,679–21,690.

Haney, M. M., Hotovec-Ellis, A. J., Bennington, N. L., De Angelis, S., & Thurber, C. (2015). Tracking changes in volcanic systems with seismic interferometry. *Encyclopedia of Earthquake Engineering*, 3767–3786.

Heliker, C., & Mattox, T. N. (2003). The first two decades of the Pu'u 'Ō'ō-Kūpaianaha eruption: Chronology and selected bibliography: Chapter 1 in The Pu'u 'Ō'ō-Kūpaianaha eruption of Kīlauea Volcano, Hawai'i: The first 20 years (Heliker, C., Swanson, D. A., & Takahashi, T. J., eds.). U.S. Geological Survey Professional Paper 1676, 28 p.

Hobiger, M., Wegler, U., Shiomi, K., & Nakahara, H. (2014). Single-station cross-correlation analysis of ambient seismic noise: Application to stations in the surroundings of the 2008 Iwate-Miyagi Nairiku earthquake. *Geophysical Journal International*, *198*(1), 90–109.

Liang, C., Karlstrom, L., & Dunham, E. M. (2020). Magma oscillations in a conduit-reservoir system, application to very long period (VLP) seismicity at basaltic volcanoes—Part I: Theory. *Journal of Geophysical Research: Solid Earth*, *125*, e2019JB017437. https://doi.org/10.1029/2019JB017437

Lin, F. C., & Farrell, J. (2018). Hawaii Nodal RAPID 2018. International Federation of Digital Seismograph Networks. Dataset/Seismic Network. https://doi.org/10.7914/SN/Z1_2018.

Lin, F. C., Li, D., Clayton, R. W., & Hollis, D. (2013). High-resolution 3D shallow crustal structure in Long Beach, California: Application of ambient noise tomography on a dense seismic array. *Geophysics*, *78*(4), Q45–Q56.

Minato, S., Tsuji, T., Ohmi, S., & Matsuoka, T. (2012). Monitoring seismic velocity change caused by the 2011 Tohoku-oki earthquake using ambient noise records. *Geophysical Research Letters*, *39*, L09309. https://doi.org/10.1029/2012GL051405

Montagna, C. P., & Gonnermann, H. M. (2013). Magma flow between summit and Pu'u 'Ō'ō at Kīlauea Volcano, Hawai'i. *Geochemistry, Geophysics, Geosystems*, *14*, 2232–2246. https://doi.org/10.1002/ggge.20145

Montgomery-Brown, E. K., Segall, P., & Miklius, A. (2009). Kilauea slow slip events: Identification, source inversions, and relation to seismicity. *Journal of Geophysical Research*, *114*, B00A03. https://doi.org/10.1029/2008JB006074

Nakata, N., Chang, J. P., Lawrence, J. F., & Boué, P. (2015). Body wave extraction and tomography at Long Beach, California, with ambient-noise interferometry. *Journal of Geophysical Research: Solid Earth*, *120*, 1159–1173. https://doi.org/10.1002/2015JB011870

Nakata, N., & Snieder, R. (2011). Near-surface weakening in Japan after the 2011 Tohoku-Oki earthquake. *Geophysical Research Letters*, *38*, L17302. https://doi.org/10.1029/2011GL048800

Neal, C., Brantley, S., Antolik, L., Babb, J., Burgess, M., Calles, K., et al. (2019). The 2018 rift eruption and summit collapse of Kīlauea volcano. *Science*, *363*(6425), 367–374. https://doi.org/10.1126/science.aav7046

Obermann, A., Planes, T., Larose, E., & Campillo, M. (2013). Imaging preeruptive and coeruptive structural and mechanical changes of a volcano with ambient seismic noise. *Journal of Geophysical Research: Solid Earth*, *118*, 6285–6294. https://doi.org/10.1002/2013JB010399

Olivier, G., Brenguier, F., Carey, R., Okubo, P., & Donaldson, C. (2019). Decrease in seismic velocity observed prior to the 2018 eruption of Kīlauea Volcano with ambient seismic noise interferometry. *Geophysical Research Letters*, *46*, 3734–3744. https://doi.org/10.1029/2018GL081609

Orr, T. R., Poland, M. P., Patrick, M. R., Thelen, W. A., Sutton, A. J., Elias, T., et al. (2015). Kīlauea's 5–9 March 2011 Kamoamoa fissure eruption and its relation to 30+ years of activity from Pu'u 'Ō'ō: Chapter 18 in Hawaiian volcanoes: From source to surface. *Geophysical Monograph*, *208*, 393–420.

Owen, S., Segall, P., Lisowski, M., Miklius, A., Denlinger, R., & Sako, M. (2000). Rapid deformation of Kilauea Volcano: Global positioning system measurements between 1990 and 1996. *Journal of Geophysical Research*, *105*(B8), 18,983–18,998.

Patrick, M., Orr, T., Anderson, K., & Swanson, D. (2019). Eruptions in sync: Improved constraints on Kīlauea Volcano's hydraulic connection. *Earth and Planetary Science Letters*, *507*, 50–61.

Patrick, M. R., Dietterich, H. R., Lyons, J. J., Diefenbach, A. K., Parcheta, C., Anderson, K. R., et al. (2019). Cyclic lava effusion during the 2018 eruption of Kīlauea Volcano. *Science*, *366*(6470), eaay9070. https://doi.org/10.1126/science.aay9070

Patrick, M. R., Orr, T. R., Swanson, D. A., Elias, T., & Shiro, B. (2018). Lava lake activity at the summit of Kīlauea Volcano in 2016, U.S. Geological Survey Scientific Investigations Report 2018–5008, 58 p.

Peng, Z., & Ben-Zion, Y. (2006). Temporal changes of shallow seismic velocity around the Karadere-Düzce branch of the north Anatolian fault and strong ground motion. *Pure and Applied Geophysics*, *163*(2–3), 567–600.

Poland, M. P., Miklius, A., & Montgomery-Brown, E. K. (2014). Magma supply, storage, and transport at shield-stage Hawaiian volcanoes: Chapter 5 in Characteristics of Hawaiian volcanoes (Poland, M. P., Takahashi, T. J., & Landowski, C. M., eds.). U.S. *Geological Survey Professional Paper*, *1801*, 179–234.

Poupinet, G., Ellsworth, W. L., & Frechet, J. (1984). Monitoring velocity variations in the crust using earthquake doublets: An application to the Calaveras Fault, California. *Journal of Geophysical Research*, *89*(B7), 5719–5731.

Qiu, H., Hillers, G., & Ben-Zion, Y. (2019). Temporal changes of seismic velocities in the San Jacinto Fault zone associated with the 2016 *Mw*5.2 Borrego Springs earthquake. *Geophysical Journal International*, *220*(3), 1536–1554. https://doi.org/10.1093/gji/ggz538

Ringler, A. T., Anthony, R. E., Karplus, M. S., Holland, A. A., & Wilson, D. C. (2018). Laboratory tests of three Z-Land FairfieldNodal 5-Hz, three component sensors. *Seismological Research Letters*, *89*(5), 1601–1608. https://doi.org/10.1785/0220170236

Schmandt, B., & Clayton, R. W. (2013). Analysis of teleseismic P waves with a 5200-station array in Long Beach, California: Evidence for an abrupt boundary to Inner Borderland rifting. *Journal of Geophysical Research: Solid Earth*, *118*, 5320–5338. https://doi.org/10.1002/jgrb.50370

Segall, P., Anderson, K. R., Johanson, I., & Miklius, A. (2019). Mechanics of inflationary deformation during caldera collapse: Evidence from the 2018 Kīlauea eruption. *Geophysical Research Letters*, *46*, 11,782–11,789. https://doi.org/10.1029/2019GL084689

Shiro, B., Burgess, M. K., Chang, J. C., Dotray, P., Okubo, P., Thelen, W. A., et al. (2018). Earthquake sequences of the 2018 Kilauea Volcano eruption. *AGU Fall Meeting Abstracts,* V41B-01.

Snieder, R., Grêt, A., Douma, H., & Scales, J. (2002). Coda wave interferometry for estimating nonlinear behavior in seismic velocity. *Science*, *295*(5563), 2253–2255. https://doi.org/10.1126/science.1070015

Snieder, R., Sens-Schönfelder, C., & Wu, R. (2016). The time dependence of rock healing as a universal relaxation process, a tutorial. *Geophysical Journal International*, *208*(1), 1–9.

Swanson, D. A., Duffield, W. A., & Fiske, R. S. (1976). Displacement of the south flank of Kilauea Volcano; the result of forceful intrusion of magma into the rift zones. U.S. Geological Survey Professional Paper 963, 44 p.

Taira, T. A., Nayak, A., Brenguier, F., & Manga, M. (2018). Monitoring reservoir response to earthquakes and fluid extraction, Salton Sea geothermal field, California. *Science Advances*, *4*(1), e1701536. https://doi.org/10.1126/sciadv.1701536

Wang, Y., Allam, A., & Lin, F.-C. (2019). Imaging the fault damage zone of the San Jacinto Fault near Anza with ambient noise tomography using a dense nodal Array. *Geophysical Research Letters*, *46*, 12,938–12,948. https://doi.org/10.1029/2019GL084835

Ward, K. M., Lin, F.-C., & Schmandt, B. (2018). High-resolution receiver function imaging across the Cascadia Subduction zone using a dense nodal Array. *Geophysical Research Letters*, *45*, 12,218–12,225. https://doi.org/10.1029/2018GL079903

Wegler, U., Nakahara, H., Sens-Schönfelder, C., Korn, M., & Shiomi, K. (2009). Sudden drop of seismic velocity after the 2004 Mw 6.6 mid-Niigata earthquake, Japan, observed with Passive Image Interferometry. *Journal of Geophysical Research*, *114*, B06305. https://doi.org/10.1029/2008JB005869

Wolfe, E. W. (1988). The Puu Oo eruption of Kilauea Volcano, Hawaii: Episode 1 through 20, January 3, 1983, through June 8, 1984. U.S. Geological Survey Professional Paper 1463, 251 p.

Woods, A. W., & Huppert, H. E. (2003). On magma chamber evolution during slow effusive eruptions. *Journal of Geophysical Research*, *108*(B8), 2403. https://doi.org/10.1029/2002JB002019

Wu, S. M., Lin, F. C., Farrell, J., & Allam, A. (2019). Imaging the deep subsurface plumbing of Old Faithful geyser from low-frequency hydrothermal tremor migration. *Geophysical Research Letters*, *46*, 7315–7322. https://doi.org/10.1029/2018GL081771

Wu, S. M., Ward, K. M., Farrell, J., Lin, F. C., Karplus, M., & Smith, R. B. (2017). Anatomy of Old Faithful from subsurface seismic imaging of the Yellowstone Upper Geyser Basin. *Geophysical Research Letters*, *44*, 10,240–10,247. https://doi.org/10.1002/2017GL075255

Yu, T. C., & Hung, S. H. (2012). Temporal changes of seismic velocity associated with the 2006 *Mw* 6.1 Taitung earthquake in an arc-continent collision suture zone. *Geophysical Research Letters*, *39*, L12307. https://doi.org/10.1029/2012GL051970

References From the Supporting Information

Farrell, J., Wu, S. M., Ward, K. M., & Lin, F. C. (2018). Persistent noise signal in the FairfieldNodal three-component 5-Hz geophones. *Seismological Research Letters*, *89*(5), 1609–1617. https://doi.org/10.1785/0220180073

Koper, K. D., & Hawley, V. L. (2010). Frequency dependent polarization analysis of ambient seismic noise recorded at a broadband seismometer in the central United States. *Earthquake Science*, *23*(5), 439–447. https://doi.org/10.1007/s11589-010-0743-5

Lin, G., Shearer, P. M., Matoza, R. S., Okubo, P. G., & Amelung, F. (2014). Three-dimensional seismic velocity structure of Mauna Loa and Kilauea volcanoes in Hawaii from local seismic tomography. *Journal of Geophysical Research: Solid Earth*, *119*, 4377–4392. https://doi.org/10.1002/2013JB010820

Moore, J. G. (2001). Density of basalt core from Hilo drill hole, Hawaii. *Journal of Volcanology and Geothermal Research*, *112*(1–4), 221–230.

Park, J., Vernon, F. L. III, & Lindberg, C. R. (1987). Frequency dependent polarization analysis of high-frequency seismograms. *Journal of Geophysical Research*, *92*(B12), 12,664–12,674. https://doi.org/10.1029/JB092iB12p12664

Erratum

In the originally published version of this article, there were minor typographical errors in the Supporting Information on lines 113 and 116 and Figure S3. These errors have since been corrected, and the present version may be considered the authoritative version of record.